Available online at www.sciencedirect.com
SCIENCE DIRECT
International Journal of Fatigue 28 (2006) 61–72
International Journal of Fatigue
www.elsevier.com/locate/ijfatigue

Crack initiation and propagation under multiaxial fatigue in a natural rubber

N. Saintier[a,*], G. Cailletaud[b], R. Piques[b]

[a] LAMEFIP, Ecole Nationale Supérieure des Arts et Métiers, EA CNRS 2727, Esplanade des Arts et Métiers, 33405 Talence Cedex, France
[b] Centre des matériaux P.M. FOURT, Ecole Nationale Supérieure des Mines de Paris, UMR CNRS 7633, Evry cedex 91003, France

Received 25 February 2004; received in revised form 9 February 2005; accepted 23 March 2005
Available online 20 June 2005

Abstract

The ever growing use of elastomers and polymers in structures leads to the need of pertinent multiaxial fatigue life criteria for such materials. Thus, the understanding of the fatigue crack initiation micro-mechanisms and their link to the local stress and/or strain history is essential. Scanning electron microscopy and Energy Dispersive Spectroscopy (EDS) have been used to investigate those micromechanisms on a natural rubber.

Rigid inclusions were systematically found at the crack initiation. Depending on the type of inclusion (identified by EDS), cavitation at the poles or decohesion are the very first damage processes observed. Cracks orientations are compared to local principal stress orientation history, the later being obtained from finite element calculations (FE). It is shown that if large strain conditions are correctly taken into account, cracks are found to propagate systematically in the direction given by the maximal first principal stress reached during a cycle, even under non-proportional loading. A fatigue life criterion is proposed.

Keywords: Multiaxial fatigue; Crack nucleation; Crack growth; Life prediction; Rubber

1. Introduction

For several decades fatigue life prediction under multiaxial loadings has played a major role in structure design. As metallic components, elastomers components subjected to cyclic loading will fail by fatigue and appropriate fatigue life criteria are needed to prevent their fracture in service.

Two main approaches have been developed for fatigue life prediction in rubber: the crack nucleation approach and the crack growth approach. The first one aim to predict the number of cycles required to cause the appearance of a crack of a given size from the history of quantities such as stress or strain, at a point. The first known study using this approach was proposed by Whöler [1] as early as the 1860s and is still in use today. Cadwell [2] was one of the first to apply this approach to elastomers.

The crack growth approach considers that a crack pre-exist in the material and that the fatigue life depends directly on the growth of this particular crack. Rivlin and Thomas [3] were the first to apply Griffith criterion to rubber [4]. The crack growth rate is computed from the so called *Tearing Energy* T which is the change in the stored mechanical energy, per unit change in crack surface area. The tearing energy is computed for a given specimen configuration, a given crack configuration and a given loading. Changing one of those parameters imply to recompute T.

When considering fatigue life prediction under non-proportional multiaxial loading, calculating T becomes quickly unreasonable. Indeed, since no analytical solutions can be found for T under complex loading and complicated specimen geometries (such as industrial components for example), calculating T imply complete 3D finite element modeling of the crack propagation process within the structure. Moreover, it is rare to know in advance the location of the crack initiation and the question of where computing T can hardly find an answer. If the crack propagation approach can be used when the crack path is well identified (crack at interfaces for example), the crack nucleation approach seems more appropriate to evaluate

* Corresponding author. Tel.: +33 678753874; fax: +33 556845366.
E-mail address: nsaintie@lamef.bordeaux.ensam.fr (N. Saintier).

0142-1123/$ - see front matter © 2005 Elsevier Ltd. All rights reserved.
doi:10.1016/j.ijfatigue.2005.03.006

fatigue life under complex loading, especially when the crack location is part of the unknowns. This imply to identify the pertinent mechanical parameters controlling multiaxial fatigue life.

Fatigue life prediction in metallic materials has been largely investigated over the past decades and is still of major concern [5,6]. In comparison to metallic materials and despite their growing use in a wide range of industrial applications, fatigue life prediction in rubber has been very little investigated. In a recent review, Mars [7] emphasis the lack of adequate multiaxial fatigue life criteria for elastomers. He also point out the fact that too little consideration had been given to the underlying mechanisms of fatigue crack initiation [8]. The purposes of this paper are: (1) to present the micromechanisms of crack initiation under non-proportional multiaxial fatigue in elastomers and (2) to establish, from those observations, which mechanical parameters are pertinent to propose a multiaxial fatigue life criterion. The establishment, identification and validation of the criterion itself will not be presented here but can be found in [9]. In this study, fatigue life corresponds to the presence of a 1 mm crack in the structure.

2. Material and mechanical testing

The material used in this study is a vulcanized Natural Rubber (NR) *cis*-1,4-polyisoprene filled with reinforcing carbon black (see Table 1 for mechanical properties). The term 'reinforcing' refer to the increased strength and stiffness of a filled NR compared to a non-filled one. At rest and room temperature, NR is amorphous which means that there is no short distance order in the molecular chain structure. However, lowering the temperature below the crystallites fusion temperature will induce partial crystallization of the polymeric chains. Due to the particular *cis*-configuration of the natural rubber crystallization will also occur by straining the material. The level of straining necessary to induce such crystallization depends on the material itself and the testing temperature. In our case, at room temperature, this value is around 130% in simple tension.

Tensile tests were carried out on $10\times1.5\times150\ \mathrm{mm}^3$ strips of material cut from rubber sheets. A screw drive INSTRON 1122 equipped with pneumatic grips was used. Strain was measured by a LLOYD laserscan200 non-contacting extensiometer and load by a 20 daN cell. Both were recorded by a computer at a 10 Hz frequency.

Table 1
Room temperature mechanical properties

Density (g/m^3)	A shore hardness	UTS (MPa)	ε_{fail} (%)	300% elong. modulus (MPa)
1.1	48	25.3	500	7.8

Molded specimens were used for constitutive model identification and fatigue testing. Specimens geometries are shown in Fig. 1. So called 'Diabolo' specimens are designed to give an uniaxial stress state under tension and compression whereas axisymmetrical notched specimens referred as AN2 (1.75 mm notch radius) and AN5 (4.75 mm notch radius) show triaxiality levels around 0.45 and 0.35, respectively, under simple tension. The elastomer was bonded to the metal end pieces during the vulcanization process.

Fatigue tests were conducted at room temperature on a tension–compression and a pure torsion home made fatigue machine. Due to large strains and the incompressibility of the NR, simply applying a torsion angle to one end of the specimen while keeping the other on fixed would induce compressive axial stresses. The torsion fatigue machine was designed to prevent those axial stresses by having one end of the specimen free of displacement along the torsion axis. Tests were performed under linear or angular displacement control with a sinusoidal waveform at a frequency of 1 Hz. Finally, so called tension–compression and static torsion fatigue tests were performed. They consist in tension–compression test, an angular pre-straining being initially applied to one end of the specimen and kept constant for the test duration.

3. Numerical procedure

As the full understanding of the crack propagation mechanisms suppose a good understanding of the large strain particularities, the following section describe the large strain formalism and present the constitutive model used in this study.

3.1. Surface and volume transport: large strain formulation

Let consider the motion $\vec{x} = \Phi(\vec{X}, t)$ of a general body in three dimensions, where a particle, initially at a position $\vec{X}$, occupies position $\vec{x}$ at time t. If we denote by $\underset{\sim}{\mathbf{F}}(X,t)$ the transformation gradient:

$$\mathrm{d}\vec{x} = \underset{\sim}{\mathbf{F}}(X,t)\mathrm{d}\vec{X} \tag{1}$$

$$\text{with } F_{iJ} = \frac{\mathrm{d}x_i}{\mathrm{d}X_J} \tag{2}$$

In the case of a general 3-dimensional motion, surface and volume in the initial and actual configuration are related by:

$$\vec{n}\mathrm{d}S = J\cdot\underset{\sim}{\mathbf{F}}^{-T}\cdot\vec{N}\mathrm{d}S_0 \tag{3}$$

$$\mathrm{d}v = J\cdot\mathrm{d}v_0 \tag{4}$$

$$J = \det(\underset{\sim}{\mathbf{F}}) \tag{5}$$

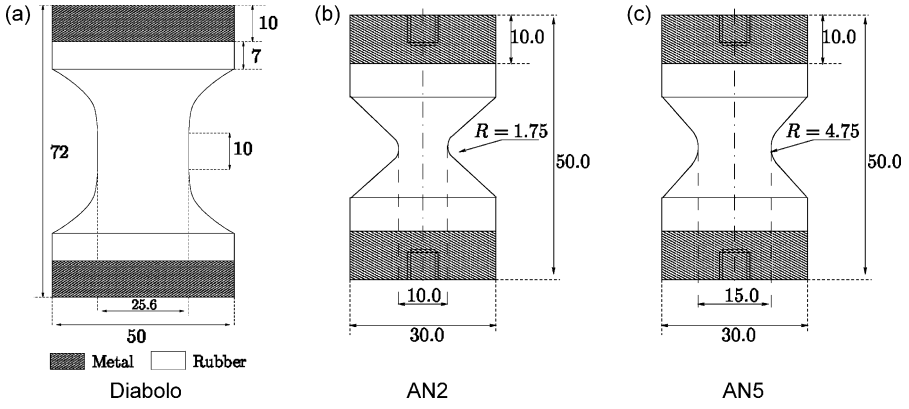

Fig. 1. Specimens geometries used for fatigue tests (dimension in mm).

where dS_0 and dv_0 are the element of surface and volume in the initial configuration. $\vec{N}$ and $\vec{n}$ are, respectively, the initial and actual normals. In the particular case of rubber elasticity, the transformation is purely isochoric (volume preserving) so that $J=1$. In the following sections those equations will be used to describe what we will call the 'material rotations', the large rotations that a material plane undergo under large strain conditions.

3.2. Strain and stress tensors

In the actual configuration, the strain tensor also called the Euler–Almansi tensor and noted $\underset{\sim}{\mathbf{A}}$ is given by:

$$\underset{\sim}{\mathbf{A}} = \frac{1}{2}(\underset{\sim}{\mathbf{I}} - \underset{\sim}{\mathbf{B}}^{-1}) \tag{6}$$

where $\underset{\sim}{\mathbf{B}} = \underset{\sim}{\mathbf{F}} \cdot \underset{\sim}{\mathbf{F}}^{-T}$ is the left Cauchy–Green tensor. In the initial configuration, the so-called Green–Lagrange strain tensor $\underset{\sim}{\mathbf{E}}$ is expressed as follow:

$$\underset{\sim}{\mathbf{E}} = \frac{1}{2}(\underset{\sim}{\mathbf{C}} - \underset{\sim}{\mathbf{I}}) \tag{7}$$

where $\underset{\sim}{\mathbf{C}} = \underset{\sim}{\mathbf{F}}^{T} \cdot \underset{\sim}{\mathbf{F}}$ is the right Cauchy–Green tensor.

In the actual configuration, the stress tensor is known as the Cauchy stress tensor. Most non-linear hyperelastic models are based on the formulation of a strain energy density W which is related to the Cauchy stress tensor (T) via the first principle of thermodynamics. The stress tensor is obtained by differentiating the strain energy function with respect to the left Cauchy–Green tensor $\underset{\sim}{\mathbf{B}} = \underset{\sim}{\mathbf{F}} \cdot \underset{\sim}{\mathbf{F}}^{T}$ as:

$$\underset{\sim}{\mathbf{T}} = 2\rho \underset{\sim}{\mathbf{B}} \frac{\partial W}{\partial \underset{\sim}{\mathbf{B}}} \tag{8}$$

where ρ is the density. Unless specified, the term of stress will always refer to Cauchy stresses.

3.3. Strain energy density

The constitutive model would not be complete without the formulation of the strain energy density. Under simple tension, the material has an hyperelastic and non-linear behavior. Tensile tests were performed along and normally to the rolling direction. No noticeable difference was found and the material behavior was considered isotropic. In the range of stress and strain considered in this study, the total dissipation under cyclic loading was less than 5% of the total strain energy. Moreover, all tests were performed at low frequency (1–2 Hz) so that no frequency effect was observed on the behavior of the material. As a consequence, a simple hyperelastic approach was chosen. A largely used model for rubbers is the one firstly proposed by Mooney and then generalized by Rivlin. It is expressed as follow:

$$W(I_1, I_2, I_3) = \sum_{i,j,k=0}^{\infty} (C_{ijk}(I_1 - 3)^i (I_2 - 3)^j (I_3 - 1)^k) \tag{9}$$

where W is the strain-energy density and I_1, I_2, I_3 are the first three invariants of the Green deformation tensor. Since the NR used is incompressible (or very nearly so), $I_3 = 1$ and the previous expression can be reduced to:

$$W(I_1, I_2) = \sum_{i,j=0}^{\infty} (C_{ij}(I_1 - 3)^i (I_2 - 3)^j) \tag{10}$$

For the type of loading encountered in this study, material stress–strain properties were found to be well described by:

$$W(I_1, I_2) = C_{10}(I_1 - 3) + C_{01}(I_2 - 3) + C_{11}(I_1 - 3) \times (I_2 - 3) + C_{20}(I_1 - 3)^2 + C_{30}(I_1 - 3)^3 \tag{11}$$

3.4. Identification

Material parameters have been identified on experimental load–displacement curves from simple tensile tests on strips of material but also from tension–compression tests on Diabolo specimens. Since no analytical model could

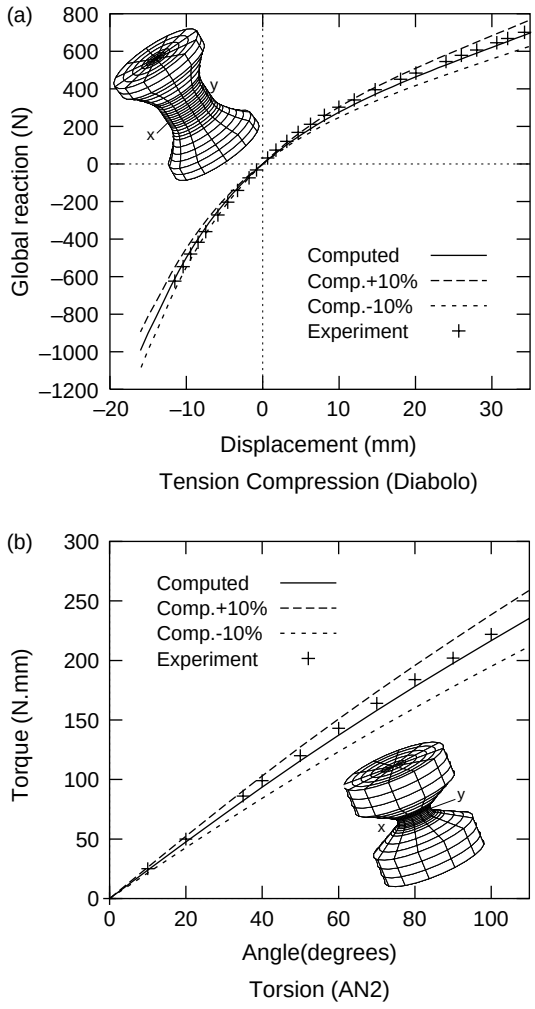

Fig. 2. Comparison between computed and experimental behavior.

describe this set of experiment, an inverse method was used. FE calculations were coupled to an optimizer to identify material parameters from experimental load–displacement curves. Both FE computations and the optimization loop were driven by the FE code ZeBuLoN [10] developed at the laboratory. As most of the elastomers, NR is known to soften under cyclic loading. Also known as the Mullins effect [11], this strain softening was found to occur during the first hundred cycles, after which the material behavior is stabilized. The identification process was performed on a stabilized material. Experimental and optimized numerical stress–strain curves are shown in Fig. 2. The optimized set of parameters are $C_{10}=0.284$, $C_{01}=0.105$, $C_{11}=0.106\times 10^{-2}$, $C_{20}=0.237\times 10^{-2}$, $C_{30}=0.104$.

4. Micromechanisms of crack initiation

Specimen surfaces were systematically observed using a field effect Zeiss scanning electron microscope (SEM) equipped with energy dispersive spectroscopy analysis facilities (EDS). The EDS analysis system works as an integrated feature of a scanning electron microscope. The technique utilizes X-rays that are emitted from the sample during bombardment by the electron beam to characterize the elemental composition of the analyzed volume. In addition, sections were cut using a cryogenic microtome (so that a perfect sectioning was ensured) to identify crack initiation mechanisms beneath the lateral surface.

4.1. Flaws at crack initiation

As classically observed in fatigue, cracks were found to initiate from existing flaws in the material, more precisely inclusions or agglomerates. Despite systematic investigation no cracks were found to initiate from pre-existing voids or surface imperfection. EDS analysis reveal that a large variety of inclusions are present in NR. The most often encountered are SiO_2 and $CaCO_3$. They are introduced in the material composition to ensure processability. However, some more 'exotic' inclusions were also identified such as natural fibers or carbon-based inclusions which can be seen as the evidence of the natural origin of the elastomer. Agglomerates result from inhomogeneous mixing during material processing. In our particular case, they are composed of carbon black (submicronic diameter) and ZnO_2 particles (size of a few microns) sticking together to finally create a 100–300 μm diameter inclusion. The rubber matrix percolates totally these agglomerates. At the difference of rigid inclusion such as SiO_2 and $CaCO_3$, agglomerates do not show a clear interface with the elastomer matrix. Instead, they have to be seen as localized highly concentrated carbon black and ZnO_2 zones in the elastomer matrix resulting in a local higher modulus and a local inclusion like behavior. It has to be noticed that those agglomerates can hardly be avoided by any type of mixing process.

4.2. Fatigue damage initiation

Two main mechanisms were found to occur at crack initiation independently of the type of loading (i.e. uniaxial or multiaxial) but depending on the nature of the inclusion: decohesion and cavitation. The distinction between decohesion and cavitation was made using SEM inspection at the crack initiation location.

4.2.1. Decohesion

The decohesion process can clearly be identified on the fracture surfaces since the surface of the inclusion, after decohesion, is free of rubber. Decohesion was found to be predominant at rigid inclusions such as SiO_2 and $CaCO_3$. Among the inclusion, the rubber matrix and the interface, the latter is clearly the weakest since no particular chemical treatments have been performed in order to improve the interface toughness. Then, the fatigue damage initiates at

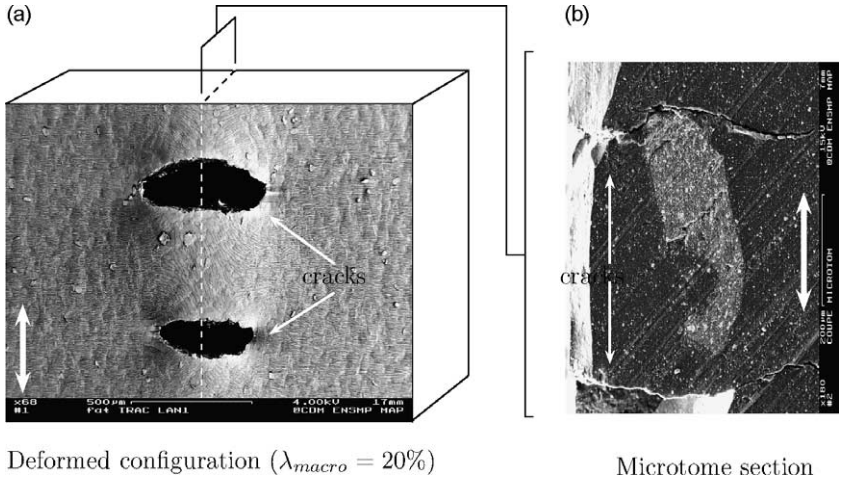

Fig. 3. Crack initiation under uniaxial fatigue loading.

the interface which leads to the decohesion between the matrix and the inclusion.

4.2.2. Cavitation

Cavitation is the process of spontaneous void nucleation under a given stress state. Cavitation was found to occur at agglomerates. Fig. 3 represents a crack at initiation after a tension–compression test on a Diabolo and the corresponding microtome section. EDS analysis and high resolution SEM imaging reveal the presence of a ZnO_2/carbon black agglomerates in between the two cracks and evidences of cavitation at the pole of the agglomerate (see Fig. 4). Hou and Aberyartne [12] proposed a cavitation model for multiaxial loading with a cavitation surface defined by:

$$S:(4\sigma_1-\sigma_2-\sigma_3)(4\sigma_2-\sigma_1-\sigma_3)(4\sigma_3-\sigma_2-\sigma_1)-(5\mu)^3=0 \quad (12)$$

where $\sigma_i(i=1,2,3)$ are the principal stresses and μ the shear modulus. This model predicts cavitation in an elastomer matrix subjected to a multiaxial loading but no cyclic effect is taken into account. It has to be notice that, according to this criterion, both the hydrostatic and deviatoric parts of the stress tensor play a role in the cavitation process which is not the case for more simple criterion such as the one proposed earlier by Gent [13]. Then, it is not expected to give an accurate prediction of stress level needed to induce cavitation under fatigue loading. Still it can provide informations concerning the nucleation location. A cell calculation has been performed. A cell contains a rigid inclusion surrounded by a rubber matrix. Periodic boundary conditions are applied. A vertical displacement is applied at the top section of the cell, simulating a tensile test. The cavitation model has been implemented in the ZeBuLoN code. The onset of cavitation correspond to the instant at which a Gauss point in the cell first reach the condition given by Eq. (12). The model was found to locate correctly the void nucleation at the pole of the inclusion but the computed minimum stress value for cavitation did not match the experimental value (i.e. cavitation was observed at lower stress levels than the computed one). It has to be noticed that the inclusion shape and modulus influence strongly the stress at cavitation. The difference between the computed and observed values of stress at cavitation can be explained by the difference between the real inclusions shape (hard to describe analytically considering the wide range of shapes and types of inclusions) and the ideal spherical inclusion taken for the calculations. In addition, due to cyclic loading, the stress softening, which may occur differently in the rubber matrix around the inclusion than it does at a macroscopic level so that the pertinent material parameter at the inclusion scale might be slightly different from those identified macroscopically. The reason why no decohesion occurs is simply that no real interface exits. Stress levels necessary to cavitation can then be reached before any stress relaxation due to decohesion occurs. In the eventuality of an increased inclusion-matrix toughness

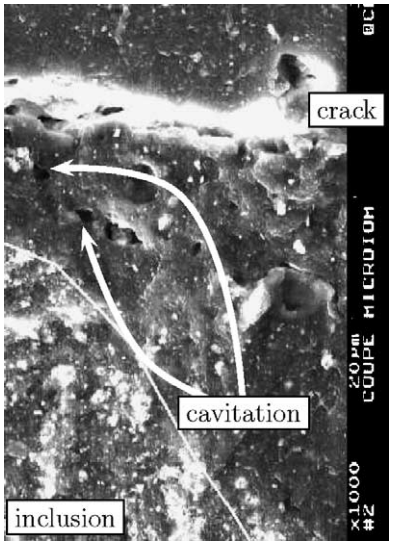

Fig. 4. Cavitation at the pole of the inclusion.

properties cavitation would become the predominant damage initiation mechanism.

4.2.3. Micro-propagation

The existence of two different mechanisms did not lead to a noticeable difference in terms of number of cycles to crack initiation. In order to estimate the percentage of the fatigue life spent in propagating the fatigue crack from 100 to 200 μm initial flaw to our critical crack size of 1 mm, further SEM investigations were performed on specially shaped thin specimens (thickness of approximately 2 mm). The specimens were designed in order to obtain a smooth stress gradient under simple tension. Specimens were tested under cyclic tension at loading ration $R=0$. The test was stopped as soon as a crack of a 1 mm size was observed. Using SEM observation it was possible to locate several microcracks. The crack length and crack location were measured. Cracks starting from the edges of the specimen were not taken into account. The predicted fatigue life at any point of the specimen surface was computed using finite element analysis and the fatigue damage model proposed in the following section. It was then possible to correlate the crack length to the percentage of total fatigue life. Five specimens were tested and 30 microcracks were obtained. As shown in Fig. 5, approximately 80% of the fatigue life is spend in propagating the crack from this 100/200 μm initial flaw to our critical crack size of 1 mm. Then the fatigue life modeling problem has more to do with how cracks propagate under non-proportional multiaxial stresses rather than how cracks nucleate.

5. Crack propagation mode

This section focus on fatigue crack propagation directions of small cracks ($L_{\text{crack}}=1$ mm) under uniaxial and non-proportional multiaxial loading. The aim is to establish the existence or not of preferred propagation mode. In the following sections, $\theta\vec{n}$ denotes the material plane angle and θ the angle between the first (i.e. maximum positive)

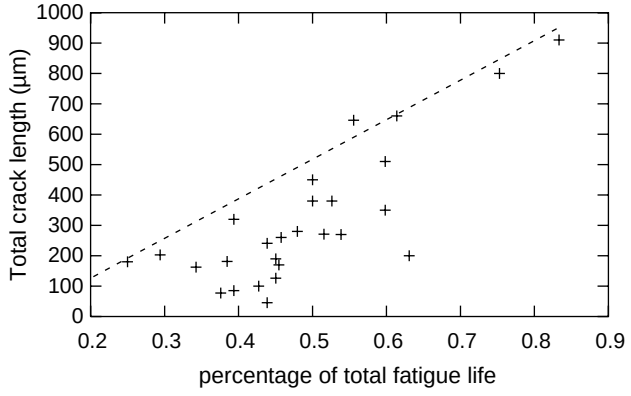

Fig. 5. Percentage of total fatigue life as a function of crack length under uniaxial loading ($R=0$).

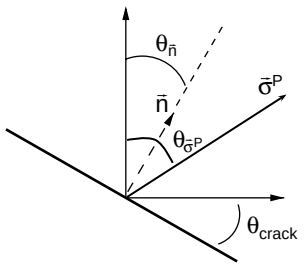

Fig. 6. Measured ($\theta\vec{n}$) and computed ($\theta_{\vec{\sigma}^P}$) angles.

Principal Stress Direction and the specimen axis (see Fig. 6). Three types of fatigue loading will be presented in details: uniaxial push–pull tests, $[0;\theta]$ torsion on AN2 and push–pull with static torsion fatigue on Diabolos.

5.1. One-dimensional loading

As shown Fig. 3, under uniaxial push–pull fatigue test, cracks were found to propagate normally to the tensile direction. This was observed for tests at positive and negative loading ratios (R ratios are varying in the range $[-2{:}.15]$), for the three types of specimens. In this simple case, the preferred crack propagation mode is an opening mode also called mode I.

5.2. Multiaxial loading

Multiaxial fatigue under large strain conditions leads to both Principal Stress Direction Rotations (PSDR) and material rotations.

5.2.1. PSDR

Principal stress direction (PSD) are easily computed for the three principal stresses since they are given by the eigen vectors of the Cauchy stress tensor. In the following section, PSD and PSDR refer to the first principal stress only.

PSDR computations at the notch root of a AN2 specimen under torsion are given Fig. 7. At small torsion angle

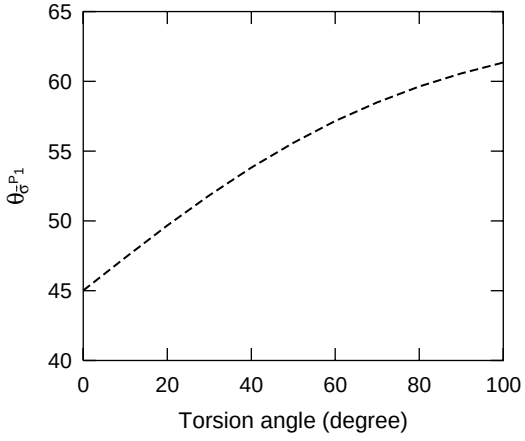

Fig. 7. Rotation of the maximal principal stress direction for a torsion test on AN2 specimens.

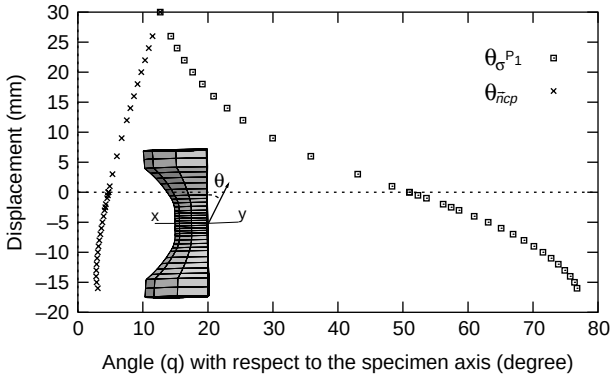

Fig. 8. Critical plane and first principal stress orientation evolutions during one cycle for a tension–compression and 60° static torsion test. Results are given for a node at the surface of the specimen.

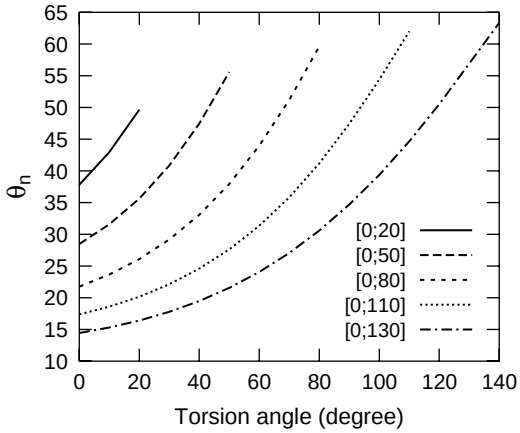

Fig. 9. Material plane rotations on AN2 specimens for different torsion tests and arbitrary initial plane orientations.

the well known PSD value of $\theta_{\sigma^p} = 45°$ is found. Increasing the torsion angle makes θ_{σ^p} to deviate from this small strain condition value. θ_{σ^p} increases up to 60° for a 100° torsion angle. It has to be pointed out hat even a simple torsion test induce strong PSDR so that it has to be considered as a non-proportional fatigue test.

Fig. 8 shows the evolution of the PSD over a cycle for a push–pull and static torsion test. The angle initially applied to the head of the specimen is 60°. Calculations are made for a node at the surface of the Diabolo where the torsion effect is the strongest. At zero axial displacement, PSD is close to 50° due to the static loading. Under axial fatigue loading, strong PSDR are observed with amplitudes up to 60°.

5.2.2. Material rotations

'Material rotations' are the rotations that undergo physical planes (for example a crack) under large strain conditions. To visualize those rotations, let us consider a cylinder of rubbery material. If a line is drawn at its surface, along the axis direction, twisting the cylinder with a large twist angle will induce a rotation of this line. In the same way, for multiaxial fatigue under large strain conditions, the orientation of a physical or material plane will undergo strong rotations over a cycle. It has to be pointed out that material rotations are generally different from PSD ones except in some particular simple cases. Since, the orientation of a material plane is given by its normal, material rotations are described by Eq. (3). In order to keep, the norm of the vector equal to one when transported from initial to deformed configuration Eq. (3) has to be modified as follow:

$$\vec{n}_t = \underset{\sim}{\mathbf{F}}_t^{-T} \odot \vec{n}_{t_0} \tag{13}$$

where the operator $\odot$ is the so called operator of normalized transport defined by:

$$\underset{\sim}{\mathbf{T}} \odot \vec{u} = \frac{\underset{\sim}{\mathbf{T}} \cdot \vec{u}}{|\underset{\sim}{\mathbf{T}} \cdot \vec{u}|} \tag{14}$$

$\underset{\sim}{\mathbf{T}}$ being a tensor and $\vec{u}$ a vector.

Material rotations have been computed accordingly to Eq. (13) for torsion tests on AN2 specimens. Results of $\theta_{\vec{n}}$ evolution as a function of the torsion angle and for different initial $\theta_{\vec{n}}$ values are reported in Fig. 9. For more clarity, the torsion angle was kept in a range where $\theta_{\vec{n}}$ values do not exceed 65°. Material plane rotations appear to be very sensitive to the initial plane orientation. The rotation amplitudes are found to be much greater than PSDR ones. For example, a material plane at a 15° angle in undeformed configuration will be at about 61° angle after a 100° torsion angle which makes an amplitude of 56°. For the same test, PSDR amplitude is only 17°.

For the previously discussed static torsion and tension-compression loading, material rotation amplitudes are found to be of approximately 5° while PSDR amplitude reach 70° (see Fig. 8).

5.2.3. Crack orientations and PSD

In order to identify, an eventual preferred crack propagation mode under multiaxial fatigue loading cracks orientations have been measured and compared to the computed PSD. Indeed, from uniaxial results and crack orientation at the notch root of an AN2 specimen under torsion (see Fig. 10) the maximum principal stress was believed to play a major role in the crack propagation process.

Fatigue tests were stopped at crack initiation and crack orientation measured using SEM observations. From FE calculation, it was possible to locate the closest node from the initiation site and then the local material rotations and PSD history. However, due to large strains, some precautions have to be taken when comparing PSD to measured crack angles.

Let us consider a general mutiaxial fatigue loading. As a crack can be considered as a material plane (it will follow the material rotations imposed by the surrounding material), we will consider that its orientation is given by its normal and that Eq. (13) can be applied. Under small strain conditions,

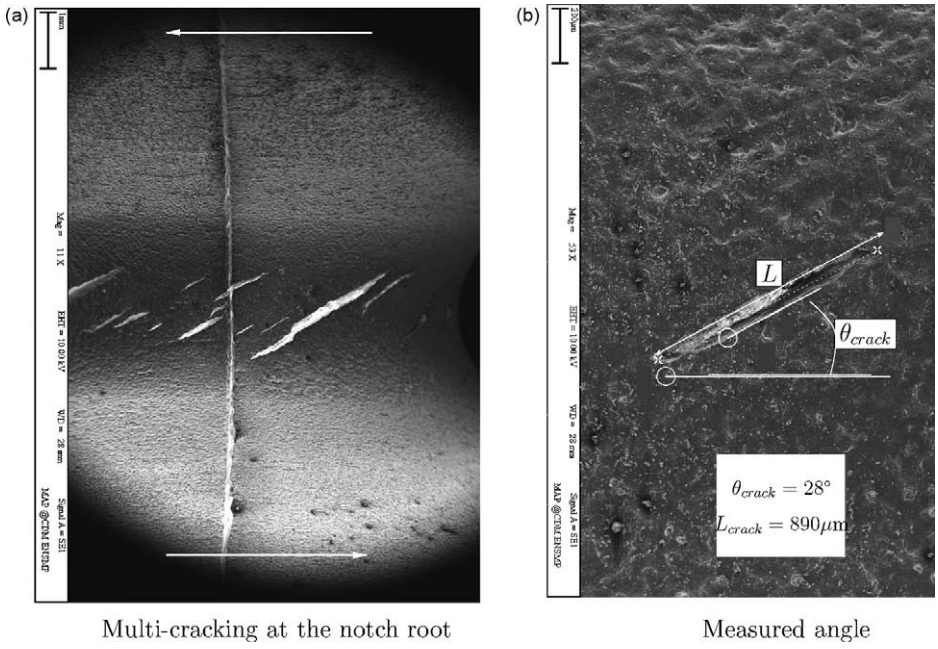

Fig. 10. Cracks at the notch (AN2) after a fatigue torsion test.

material rotations are so small compared to principal stress direction rotations that crack orientation measurements can be directly compared to computed principal stress directions. Under large strain conditions, both principal stress directions and material planes directions rotate. Since crack orientation measurements are usually done in the undeformed configuration whereas principal stress direction orientations are computed in the deformed (i.e. actual) configuration, they cannot be directly compared. Before comparison, they have to be transported in the same configuration. The easiest way of doing so is to consider an eigen stress vector as a normal $\vec{n}_{\text{actual}}$ to a material plane and use Eq. (13) to evaluate the corresponding normal $\vec{n}_{\text{undeformed}\leftarrow\text{actual}}$ in the undeformed configuration.

Also, the stress history on a given plane can be expressed in terms of normal ($\sigma_{\vec{n}_t}$) and shear stress ($\tau_{\vec{n}_t}$) as follow:

$$\sigma_{\vec{n}_t} = \vec{n}_t \cdot \underline{\sigma}(t) \cdot \vec{n}_t \tag{15}$$

$$\tau_{\vec{n}_t} = \sqrt{|\underline{\sigma}(t) \cdot \vec{n}(t)|^2 - (\vec{\sigma}_{\vec{n}_t})^2} \tag{16}$$

5.2.4. Alternate torsion loading

A 0–100° torsion test is taken as an example to describe the procedure performed at each node of the structure:

(i) the time $t_{\max}$ at which the maximum first principal stress is reached is identified,
(ii) the corresponding eigen vector is transported in the undeformed configuration using Eq. (13),

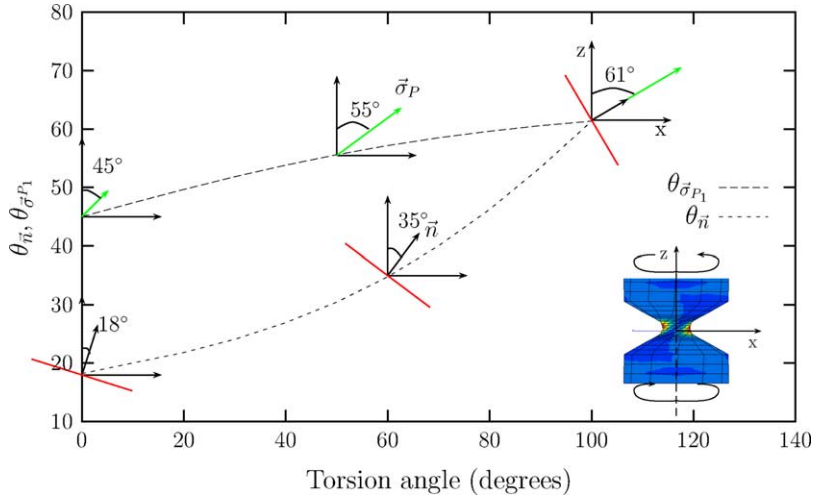

Fig. 11. Comparison between $\vec{\sigma}^{P_1}$ rotation and material rotations for a 0–100° torsion test.

(iii) the predicted and measured crack angles are compared.

The procedure is shown in Fig. 11 for a [0; 100] alternate torsion test. In this case, the PSD angle at t_{max} is 61°. The corresponding material plane angle in the undeformed configuration is 18°. This 18° computed angle will be compared to measured crack angle. It demonstrates clearly the need of taking into account material plane rotation.

The procedure was applied for all alternate torsion tests performed in this study. As we are dealing with notched specimens, cracks were not found to initiate strictly at the notch root but rather in a 1 mm band centered on the later. Therefore, computed angles were obtained for two nodes, one at the notch root and the second one located at 500 μm away from it. Results are given in Fig. 12. The procedure was applied to AN5 and Diabolos specimens with the same success in predicting crack orientations.

It shows that, for these loading conditions, the crack orientation is given by the maximal first principal stress direction reached during a cycle. Moreover it demonstrates that the crack initiation orientation depends not only on the type of loading applied to the specimen (i.e. torsion, combined tension torsion, etc) but also on the level of loading applied.

5.2.5. Fully reverse torsion loading

Fully reverse torsion tests $[+\theta;\ -\theta]$ were also conducted (θ is the angular displacement applied to the specimen ends). In this particular case, the symmetry of the loading implies that the loading history on the two planes at $+\theta_{\vec{n}}$ and $-\theta_{\vec{n}}$ are 90° out of phase but with the same amplitudes. For a given $[+\theta;\ -\theta]$ two planes experience the same maximum first principal stress, at orientations $+\theta_{\vec{n}}$ and $-\theta_{\vec{n}}$. Experimentally cracks were found to initiate perpendicularly to the specimen axis independently of the level of loading applied to the specimen and the fatigue life

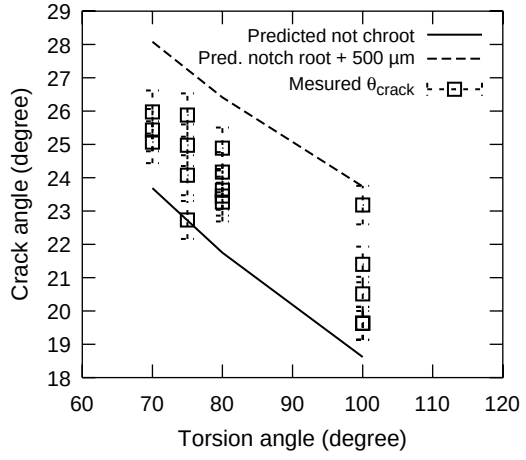

Fig. 12. Comparison between predicted and measured crack orientations, material plane rotation being taken into account.

was half the one observed for the corresponding [0; θ] alternate torsion fatigue test. In order to better understand this phenomenon, fatigue tests were conducted by blocks of 1000 cycles, each block consisting in 500 cycles at $[0;+\theta]$ followed by 500 cycles at $[0;-\theta]$. The crack path was identified using SEM. A zig–zag like crack propagation was observed with characteristic angles close to those observed under simple [0; $+\theta$] and [0; $-\theta$] torsion tests. Those results show that the 90° angle crack propagation observed under fully reversed torsion is the result of a micro zig–zag like propagation at each cycles giving globally a crack orientation of 90°. Since, over one cycle, the crack propagates once at $+\theta_{\vec{n}(t_{max})}$ and once at $-\theta_{\vec{n}(t_{max})}$ this also explain why the fatigue life of an alternate torsion loading is twice the one of a fully reverse torsion loading (test being conducted at the same maximum level).

5.2.6. Push–pull and static torsion loading

Despite the static torsion angle, fatigue cracks were found to initiate and propagate quasi normally to the tensile direction with only a 1–2° angle. As done previously for the torsion test, PSDR and material plane rotation have been computed and are reported in Fig. 8 for a node at the surface of the Diabolo. The PSD is found to be equal to 15° in the maximally deformed position. The corresponding material plane angle is equal to 5° when the specimen is unloaded. In this case, cracks were found to initiate from the inside of the specimen, at a characteristic distance from the surface. The reason why such a phenomenon occur is beyond the scope of this paper but can be found in [9]. At this particular location the computed crack angle value is 2° (the static torsion effect is weaker). This value is in accordance with the quasi normal fracture surface observed experimentally.

6. Fatigue life prediction

It is well known that for uniaxial fatigue testing on natural rubber, running tests at positive loading ratio induce a strong increase in the fatigue life. This was observed by many authors [2,14] and explained as the result of the strain induced crystallization ability of rubber (synthetic rubber which do not show such an ability do not present this reinforcement at $R>0$ either). We propose to correlate the fatigue life to an equivalent quantity Φ_{eq} defined as follow:

$$\Phi_{eq} = \frac{\Phi_{damage}}{1 + \Phi_{reinforcement}} \tag{17}$$

where Φ_{damage} (resp. $\Phi_{reinforcement}$) is the driving force of the damage process (resp. reinforcement process). $\Phi_{reinforcement}$ is positive under reinforcing loading condition and null otherwise. If the condition for having reinforcement under uniaxial loading is simple ($R>0$), it becomes much more complex under multiaxial loading. For this reason, the way of computing $\Phi_{reinforcement}$ will be published in a paper to

come. Guidelines can be found in [15]. All the results presented in this section have $\Phi_{\text{reinforcement}}=0$. We will focus here on how to compute Φ_{damage}. The number of cycles to crack initiation is correlated to Φ_{eq} via a classical power law function:

$$N_i = \left(\frac{\Phi_{\text{eq}}}{\Phi_0}\right)^{\alpha} \tag{18}$$

α and Φ_0 are material parameters to identify.

6.1. Choice of a pertinent mechanical parameter

Most existing fatigue life models are based on stress, strain, strain energy evolution or any combination of those quantities depending on the type of material studied. Mars [8], recently proposed that for rubbery materials the fatigue life could be related to an amount of energy ΔW_c, where W_c represents the so called cracking energy density defined as follows:

$$\mathrm{d}W_c = \sigma \mathrm{d}\vec{\varepsilon} = \vec{r}^t \underset{\sim}{\sigma} \mathrm{d}\underset{\sim}{\varepsilon} \vec{r} \tag{19}$$

where $\vec{r}$ is a fixed unit vector normal to the plane of interest, and $\underset{\sim}{\sigma}$ and $d\underset{\sim}{\varepsilon}$ are the stress and strain increment tensors, respectively. He considers the orientation of the plane of interest $\vec{r}$ constant over a cycle and identify the plane of crack initiation as the plane which maximizes $\Delta W_c = W_{c,\max} - W_{c,\min}$. However, it was not clear how such a quantity could be computed with an incremental definition of W_c. The fatigue life is then related to ΔW_c via a power-law function.

Under large strain conditions, not taking into account material plane rotations can be hazardous when computing an amplitude of a given quantity. Let us assume a given mechanical quantity X (stress, strain or energy), of which we want to compute an amplitude and mean stress value on a particular material plane. Since $X_{\max}$ and $X_{\min}$ must be computed at two different times the corresponding material planes are different. So, their rotations have to be taken into account and the procedure described Section 5.2.2 has to be applied.

The previously exposed methodology to find fatigue crack orientation from the principal stress directions could have been performed in the same way using principal strain directions since they coincide for an isotropic hyperelastic behavior. However, when considering isotropic incompressible hyperelastic materials such as rubber, the strain tensor is only depending on the deviatoric part of the stress tensor. By definition of incompressibility, an hydrostatic stress state does not induce any deformation. Thus, computing a damage parameter exclusively from the evolution of a strain quantity imply that the hydrostatic part of the loading does not induce any damage. This was found to be experimentally wrong [9]. For the same reason considering a damage parameter from an energy based quantity present some difficulties. As soon as a strain-based quantity tends towards zero (i.e. when the stress state becomes close to a purely hydrostatic stress state), so does the corresponding energy based quantity. There hence, we preferred use the Cauchy stress tensor history over a cycle to express the damage parameter. As the maximal principal stress direction was found to correctly predict the fatigue crack orientations under non-proportional multiaxial loading we suggest that the maximum value of the first principal stress (σ^{p_1}) reached during a cycle drives the damage process so that:

$$\Phi_{\text{damage}} = \underset{t\in[0:T]}{\text{Max}}(\sigma_n) \tag{20}$$

where T is the period of the signal and σ_n is the normal stress acting on the plane that experiences the highest maximum principal stress. This model imply that compressive stresses have no effect on the fatigue life. This is consistent with the fact that a preferred mode I crack initiation is observed and that by closing the fatigue crack, negative stresses on that particular plane have no effect on the damage process.

6.2. One-dimensional results

The two parameters of the model, α and Φ_0, have been identified on push–pull fatigue test results with compressive stresses ranging from -4 to 0 MPa. As said in the first section, tests were stopped as soon as a 1 mm crack was observed at the specimen surface. The fatigue lives are computed using Eq. (17) with $\Phi_{\text{reinforcement}}=0$ (tests with negative loading ratios). The comparison between predicted and observed fatigue life for uniaxial tests is given in Fig. 13. The proposed model predicts the observed fatigue life: the simulated life remains in a scatter band, which is reasonable. As supposed compressive stresses do not show any influence on the fatigue life for natural rubber.

6.3. Multiaxial results

Once identified on one-dimensional results the proposed model was applied to multiaxial test results where

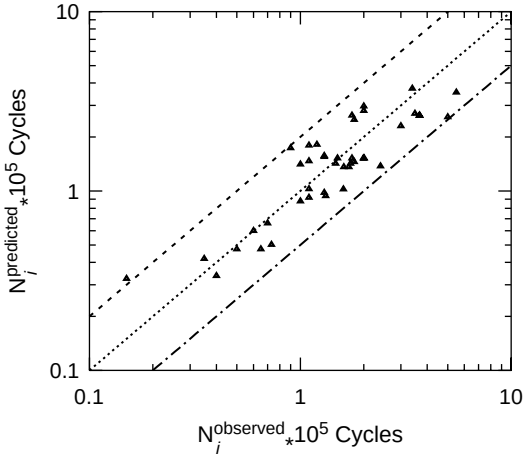

Fig. 13. One-dimensional results after identification.

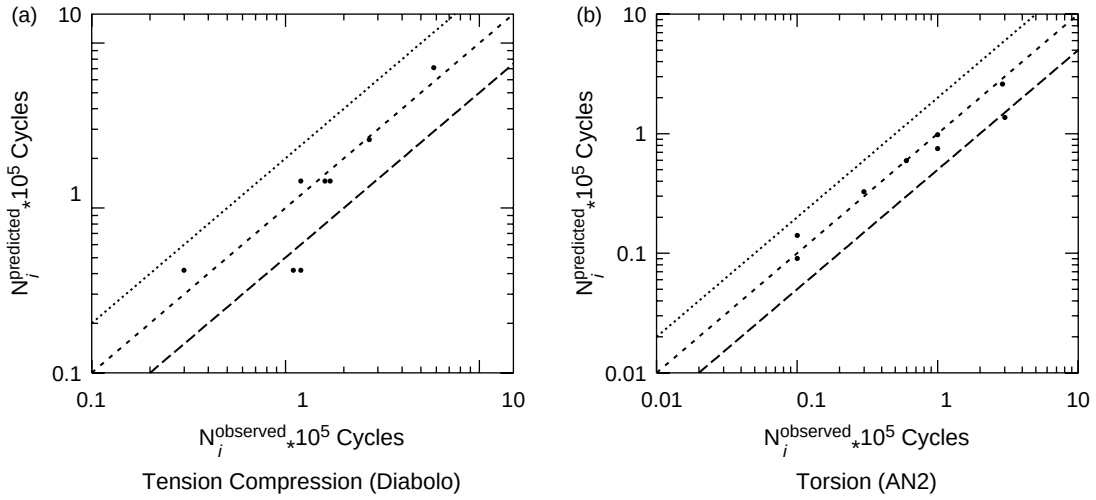

Fig. 14. Comparison between predicted and observed fatigue life.

the reinforcing condition was not met (i.e. where $\Phi_{\text{reinforcement}}=0$). Results are presented Fig. 14 for [0; θ] torsion tests on Diabolo and push-pull tests on AN5. In both cases, a good agreement is observed between predicted and computed fatigue life. Only two points seem to slightly differ from the predictions. This could be due to the fact that for those tests it can be experimentally hard not to meet reinforcing conditions.

7. Conclusions

The micromechanisms leading to the initiation of a 1 mm fatigue crack under multiaxial cyclic loading have been investigated. It was shown that cracks initiate from flaws pre-existing in the material. For the natural rubber investigated they consist in rigid inclusions like SiO_2 or $CaCO_3$ particles, and large carbon black agglomerates of an average size of 200 μm. Depending on the type of inclusion, the very first damage processes observed are decohesion or cavitation. Those mechanisms are similar to those observed under simple tension on rubbery materials. Fatigue loading in rubber does not produce new type of damage mechanisms as it does in metallic materials. It was found that 20% of the fatigue life is spent in propagating the crack from this initial 200 μm micro-crack up to our 1 mm critical size.

Crack orientations under non-proportional multiaxial fatigue loading were investigated. It was found that if material plane rotations are correctly taken into account, the direction given by the maximum first principal stress reached during a cycle correctly predicts the crack orientation in all the fatigue loading encountered in this study. Crack orientation were found to depend not only on the type of loading (tension, torsion, etc.) but also on the maximum level of loading.

A simple fatigue model was proposed, suitable for fatigue loading where no reinforcement is observed. After identification on the uniaxial data, it was found to describe correctly experimental multiaxial data. It was shown that, for hyperelastic incompressible materials such as rubber, stress based criterion are able to predict the fatigue life in the multiaxial loading cases considered in this study. The fatigue criterion has been implemented in the Zebulon FE code and is able to locate the crack initiation, predict the fatigue life and the crack orientation on structures. Compared to energy or strain based approaches, the stress based approach do not give infinite fatigue life for purely hydrostatic stress states. However, more experimental fatigue test results are needed to establish the quality of the predictions in case of highly hydrostatic stress states. It was shown that material plane rotations have to be taken into account as soon as a mean or amplitude of a given oriented quantity is computed (stress or strain normal to a plane for example).

The case of loading with reinforcement (positive loading ratio under simple tension for example) has been treated in [9] and will be presented in a paper to come.

Acknowledgements

This work was done with the financial support of PAULSTRA-HUTCHINSON.

References

[1] Wohler A. Wohler experiments on the strength of metals. Engineering 1867;2:160.
[2] Cadwell SM, Merril RA, Sloman CM, Yost FL. Dynamic fatigue life of rubber. Ind Eng Chem 1940;12:19–23.
[3] Rivlin R, Thomas A. Rupture of rubber part 1: characteristic energy for tearing. J Polym Sci 1953;10:291–318.
[4] Griffith AA. The phenomenon of rupture and flow in solids. Phil Trans R Soc Lond 1920;221:163.

[5] Papadopoulos I, Davoli P, Gorla C, Filippini M, Bernasconi A. A comparative study of multiaxial high-cycle fatigue criteria for metals. Int J Fatigue 1997;19:219–35.
[6] Papadopoulos I. Long life fatigue under multiaxial loading. Int J Fatigue 2001;23:839–49.
[7] Mars W, Fatemi A. A literature survey on fatigue analysis approaches for rubber. Int J Fatigue 2002;24:949–61.
[8] Mars W. Cracking energy density as a predicting factor of fatigue life under multiaxial conditions. Rubber Chem Technol 2002;75: 1–15.
[9] Saintier N. Multiaxial fatigue life of a natural rubber: crack initiation mechanisms and local fatigue life criterion. PhD Dissertation, Ecole des Mines de Paris.
[10] ZeBuLoN, User manual, Transvalor/ENSMP-Centre des matriaux, BP87 F-91003 Evry Cedex, www.mat.ensmp.fr.
[11] Mullins L. Effect of stretching on the properties of rubber. J Rubber Res 1947;16:275–89.
[12] Hou H, Abeyaratne R. Cavitation in elastic and elastic–plastic solids. J Mech Phys Solids 1992;571–92.
[13] Gent AN. Cavitation in rubber: a cautionary tale. Rubber Chem Technol 1990;63:G49–G53.
[14] Lindley PB. Relation between hysteresis and the dynamic crack growth resistance of natural rubber. Int J Fract 1973;9:449–62.
[15] Saintier N, Cailletaud G, Piques R. Fatigue life prediction of natural rubber components under uniaxial and multiaxial loading. Proceedings of the EUROMAT 2000 conference.